Nature Environment and Pollution Technology
An International Quarterly Scientific Journal

p-ISSN: 0972-6268
(Print copies up to 2016)
e-ISSN: 2395-3454

Vol. 25 | No. 3 | Article ID D1891 | 2026

Original Research Paper

https://doi.org/10.46488/NEPT.2026.v25i03.D1891

Open Access Journal

An Assessment of Biopolymer-Based Metal Oxide Nanoparticles for the Removal of Heavy Metals from Water

Koffi Sossou[1]†, Alfred O. Mayabi[2], Zeraebruk Negusse Kahsay[2] and Charles K. Cheruiyot[2]

[1]Department of Civil Engineering, Pan African University Institute for Basic Sciences, Technology and Innovation (PAUSTI-JKUAT), Kenya

[2]Department of Civil, Construction and Environmental Engineering, Jomo Kenyatta University of Agriculture and Technology, Nairobi, Kenya

†Corresponding author: Koffi Sossou; sossou.koffi@students.jkuat.ac.ke

Abbreviation: Nat. Env. & Poll. Technol.
Website: www.neptjournal.com

Received: 10-12-2025
Revised: 21-01-2026
Accepted: 30-01-2026

Key Words:

Adsorption
Banana peels
Kinetic study
Chemisorption
Metal oxide nanoparticles
Removal of heavy metals

Citation for the Paper:

Sossou, K., Mayabi, A.O., Kahsay, Z.N. and Cheruiyot, C.K., 2026. An assessment of biopolymer-based metal oxide nanoparticles for the removal of heavy metals from water. *Nature Environment and Pollution Technology*, 25(3), D1891. https://doi.org/10.46488/NEPT.2026.v25i03.D1891

Note: From 2025, the journal has adopted the use of Article IDs in citations instead of traditional consecutive page numbers. Each article is now given individual page ranges starting from page 1.

ABSTRACT

Water contamination by toxic heavy metals continues to be a major environmental and public health issue, requiring affordable and sustainable remediation solutions. This study developed a nanocomposite from banana peel, incorporating Fe_3O_4 and TiO_2 nanoparticles through a combined co-precipitation and hydrothermal method, and evaluated its effectiveness in adsorbing Cr(VI), Cd(II), and Pb(II) from water. Characterization techniques such as FTIR, SEM–EDS, and XPS confirmed successful integration of Fe_3O_4 and TiO_2 into the banana peel matrix, improving surface properties and magnetic separability. The adsorption data fit the Langmuir and Redlich–Peterson models best, indicating monolayer adsorption with maximum capacities of 14.4 $mg.g^{-1}$ for Cr(VI), 10.9 $mg.g^{-1}$ for Cd(II), and 100 $mg.g^{-1}$ for Pb(II). Kinetic analysis showed the adsorption follows a pseudo-second-order model (R2 = 0.97–0.93). The nanocomposite exhibited excellent adsorption efficiency and competitive capacity compared to other metal oxide adsorbents, demonstrating its potential as a low-cost, sustainable material for removing multiple heavy metals and valorizing agricultural waste.

1. INTRODUCTION

Environmental pollution resulting from inadequate wastewater management has attracted significant global attention in recent decades, particularly due to the discharge of toxic heavy metals into aquatic environments. Wastewater containing heavy metals, dyes, and organic pollutants poses serious risks to ecosystems and human health because these contaminants are non-biodegradable, persistent, and capable of bioaccumulation (Sossou et al. 2024a, A. Mishra et al. 2022). In countries with limited wastewater treatment infrastructure and weak regulatory enforcement, contamination of water resources by heavy metals is further exacerbated (Smyth et al. 2024, Strategies et al. 2024).

Conventional wastewater treatment methods, including chemical precipitation, ion exchange, and membrane filtration, often suffer from high operational costs, secondary sludge generation, and low selectivity for multiple coexisting contaminants (Razzak et al. 2022). Consequently, adsorption using low-cost and environmentally friendly materials has emerged as a promising alternative for heavy metal removal. In this context, biosorbents derived from agricultural residues have gained increasing attention because of their abundance, biodegradability, and alignment with circular economy principles.

Banana peel is one such agricultural by-product that has been extensively investigated as a low-cost biosorbent. According to the Food and Agriculture Organization of the United Nations (FAO 2024), approximately 3.5 million tonnes

of banana peel waste are generated each year globally. Much of this biomass is disposed of in open dumps or landfills, leading to environmental problems such as leachate generation, greenhouse gas emissions during decomposition, and contamination of soil and water resources (Mor et al. 2023, Sial et al. 2019). Nevertheless, banana peel contains significant amounts of cellulose, hemicellulose, lignin, pectin, and starch, which provide abundant functional groups, including hydroxyl and carboxyl moieties, capable of interacting with metal ions (Pokharel et al. 2018, Liew et al. 2018, Mehmood et al. 2025, Mishra et al. 2023). Despite these advantages, raw banana peel and unmodified biopolymers often exhibit limited adsorption capacity and reduced effectiveness in multicomponent systems because of competitive adsorption among coexisting metal ions (Gupta et al. 2025).

To overcome these limitations, the integration of metal oxide nanoparticles with biomass-based adsorbents has been widely explored. Nanomaterials such as iron oxides and titanium dioxide offer high surface areas, enhanced surface reactivity, and improved physicochemical stability, resulting in superior adsorption performance (Togun et al. 2025, Sossou et al. 2024b). In particular, magnetite (Fe_3O_4) nanoparticles are attractive because of their strong affinity for metal ions and magnetic properties, which facilitate easy separation from treated water. Similarly, TiO_2 provides additional adsorption sites and enhances the chemical stability of the composite (Lellala et al. 2024).

Despite these advances, most previous studies have focused on single-metal systems or non-magnetic banana peel modifications, limiting their applicability to real wastewater containing multiple competing contaminants. Therefore, this study aims to synthesize and evaluate a Fe_3O_4/TiO_2/banana peel nanocomposite for the removal of Cr(VI), Cd(II), and Pb(II) from aqueous solutions under multicomponent conditions. The findings provide valuable insight into the potential of this nanocomposite as a low-cost, sustainable, and environmentally friendly material for heavy metal remediation.

2. MATERIALS AND METHODS

2.1. Adsorbent's Preparation and Characterization

2.1.1. Hydrothermal-Assisted Nanocomposite Synthesis of Iron Oxide

Hydrothermal-assisted synthesis was used to produce iron oxide-based nanocomposites. Low-grade iron oxides sourced from Ollesos Company in Kenya served as raw materials without any chemical modification. A total of 100 g of the mixed iron oxide powders was dispersed in 100 mL of distilled water and stirred at 40 rpm for 2 h to create a uniform suspension. The pH was adjusted to 7 with NaOH solution. The suspension was transferred into a Teflon-lined stainless steel autoclave and subjected to hydrothermal treatment at 105°C for 12 h.

After natural cooling to room temperature, the solid product was separated by centrifugation, washed three times with ethanol, then with distilled water to eliminate impurities. The washed material was dried in an oven at 80°C and calcined at 500°C for 6 h. The calcined powder was ground with a mortar and pestle to produce a fine, homogeneous nanocomposite powder (Fig. 1).

2.1.2. Hydrothermal Synthesis of Titanium Dioxide

TiO_2 nanoparticles were synthesized via a hydrothermal method with slight modifications to previously established

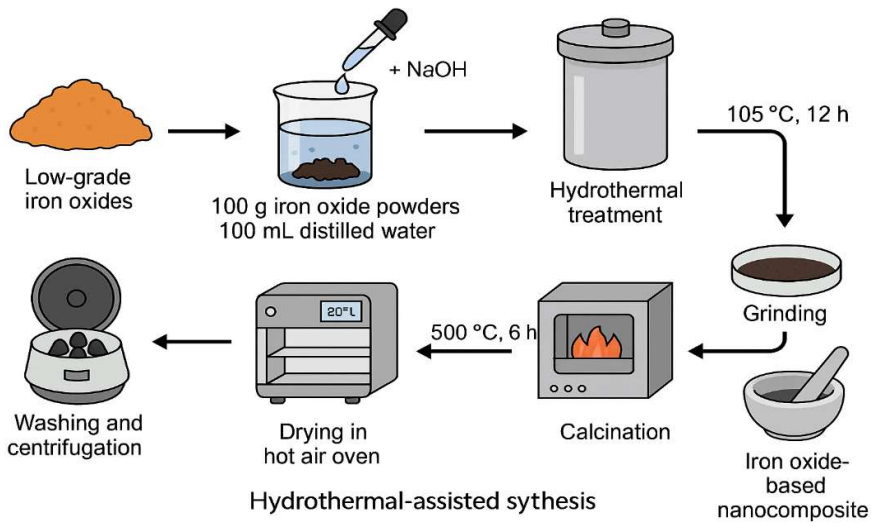

Fig. 1: Hydrothermal-assisted nanocomposite synthesis of iron oxide.

procedures (Keerthana et al. 2018, Zanganeh et al. 2011). Commercial TiO_2 powder (Degussa P25, Evonik, 99.9% purity, anatase/rutile ratio of 90:10, particle size approximately 10 nm) served as the precursor. Briefly, 1 g of TiO_2 was dispersed in 50 mL of 10 M NaOH solution under vigorous stirring for 40 minutes. The resulting suspension was transferred to a 50 mL Teflon-lined stainless-steel autoclave and heated at 200°C for 48 h.

The precipitate was then cooled to room temperature, washed repeatedly with deionized water (resistivity ≥15 MΩ·cm) and 0.1 M HCl until neutral pH was reached, and separated by centrifugation at 5000 rpm for 10 minutes. The product was dried at 60°C for 1 h and calcined at 250°C for 2 h in air to improve crystallinity and reduce residual sodium content.

To assess the influence of the alkaline medium, the synthesis was repeated using KOH instead of NaOH. The resulting TiO_2 nanoparticles were stored in a desiccator until further characterization and application.

2.1.3. Biopolymer Materials

For the biopolymer preparation, banana peels were locally obtained from Juja Market in Kenya, washed three times with tap water, and cut into small pieces measuring 3-4 cm. The peels were air-dried for one week, then baked in a hot-air oven at 105°C for 12 h. The dried peels were crushed with a mortar and pestle into a fine powder, which was sieved through a 200 µm mesh to ensure uniform particle size. This powder served as the raw material for creating a homogeneous nanocomposite. The morphology of the banana peel powder was examined using scanning electron microscopy (SEM) micrographs of the peels and biochar surfaces.

2.2. Characterization of the Materials

The nanomaterials, iron oxide, titanium dioxide, and biopolymer powder, were thoroughly characterized to assess their physical, chemical, and structural properties. Parameters such as surface area, pore size distribution, chemical composition, elemental states, and magnetic properties were evaluated. Crystalline phases were analyzed using X-ray Diffraction (XRD, Bruker D8 Advance, Germany) with Cu-Kα radiation (λ = 1.5406 Å). Elemental composition was determined via X-ray Fluorescence (XRF, PANalytical Axios, Netherlands). Surface morphology was examined with Scanning Electron Microscopy (SEM, JEOL JSM-7610F, Japan). The chemical states and elemental composition of the samples were analyzed by X-ray Photoelectron Spectroscopy (XPS, PHI 5000 VersaProbe III, ULVAC-PHI, Inc., Japan) under ultra-high vacuum (~2×10^{-7} Pa). A monochromatic Al Kα X-ray source (hν = 1486.6 eV) with a 100 µm beam diameter was used. Survey scans employed a pass energy of 280 eV, while high-resolution scans used 55 eV with a step size of 0.05 eV. Raster scanning was performed on the samples with the stage tilt fixed at 45°. Charge neutralization was achieved using a neutralizer set at 1.5 V and 20 µA. The analysis was conducted at a base pressure of approximately 8×10^{-8} Pa. Samples were affixed using non-conductive tape. Data acquisition and peak deconvolution were carried out with Multipak software.

2.3. Preparation of Heavy Metal Stock Solutions

All chemicals utilized in this study were of analytical grade (≥99.5%, 200 mesh) and were obtained from Merck and Sigma-Aldrich. Precise amounts of potassium dichromate ($K_2Cr_2O_7$), cadmium nitrate [$Cd(NO_3)_2$], and lead nitrate [$Pb(NO_3)_2$] were carefully weighed and dissolved in distilled water (resistivity ≥15 MΩ·cm) to create a mixed heavy-metal stock solution containing 50 $mg.L^{-1}$ of Cr(VI) and Cd(II), and 10 $mg.L^{-1}$ of Pb(II). The exact mass of each metal salt was calculated for accuracy. All experiments were conducted at room temperature (298 ± 2 K) under atmospheric pressure. The pH of the solutions was adjusted as necessary using hydrochloric acid (HCl) or sodium hydroxide (NaOH).

2.4. Adsorption Experiments

Batch adsorption experiments involved adding a specified mass of Fe_3O_4/TiO_2–banana peel nanocomposite (0.5–2.5 g) to a series of 250 mL conical flasks containing 100 mL of mixed heavy-metal solution with an initial concentration of 50 $mg.L^{-1}$ (C_o). The flasks were placed on a magnetic stirrer and stirred at 90 rpm for 60 minutes to facilitate adsorption. After each run, the supernatant was carefully withdrawn, filtered through Whatman No. 42 filter paper, and analyzed for residual concentrations of Cr (VI), Cd (II), and Pb (II) (Ct) using Atomic Absorption Spectroscopy (AAS).

The amount of metal ions adsorbed, denoted as qt ($mg.g^{-1}$), was calculated using Eq. 2 (Otieno et al. 2021)

$$q_t = \frac{(Co - Ct)}{W} V \quad \ldots(1)$$

Where C_o and C_t are the metal ion concentrations ($mg.L^{-1}$) initially and at the end of the run, respectively, V is the solution volume (mL), and W is the mass of the adsorbent (g).

2.5. Adsorption Isotherms

Adsorption isotherms were employed to analyze the equilibrium data obtained from the batch experiments. The data were modeled using nonlinear Langmuir and Freundlich isotherm equations (Eqs. 2 and 3). The nonlinear formulation was favored over the linearized versions to reduce errors from

data transformation and to ensure more precise and reliable parameter estimation.

The Langmuir isotherm model describes monolayer adsorption on a homogeneous surface with a finite number of identical active sites, and is expressed as:

$$q_e = \frac{q_{max} K_L C_e}{1 + K_L C_e} \quad \ldots(2)$$

Where:

- q_e (mg.g^{-1}) is the amount of adsorbate adsorbed at equilibrium,
- C_e (mg.L^{-1}) is the equilibrium concentration of cadmium in solution,
- q_{max} (mg.g^{-1}) is the maximum adsorption capacity,
- K_L (L.mg^{-1}) is the Langmuir constant related to adsorption affinity.

The Freundlich model describes multilayer adsorption onto heterogeneous surfaces and is given by:

$$q = K_F C_e^{1/n} \quad \ldots(3)$$

Where:

- K_F (mg.g^{-1}) (L.mg^{-1})$^{1/n}$ is the Freundlich constant indicating adsorption capacity,
- n is the heterogeneity factor, with 1/n representing adsorption intensity.

The suitability of each model was assessed by correlation coefficients (R^2) and error functions.

2.6. Adsorption Kinetics

Kinetic experiments were carried out to examine the rate and mechanism of adsorption of Cr (VI), Cd(II), and Pb(II) onto the synthesized Fe_3O_4/TiO_2/banana peel nanocomposite. Batch studies were conducted with four different adsorbent dosages (0.5, 1, 1.5, 2, and 2.5 g), maintaining an initial metal ion concentration of 50 mg.L^{-1} for Cr(VI) and Cd(II), and 10 mg.L^{-1} for Pb(II). The solution volume was 100 mL, with a natural pH range of 6.0 to 6.5. For each contact time, identical 250 mL conical flasks containing the same solution and adsorbent dose were prepared to ensure consistent conditions. These flasks were stirred at 90 rpm using a magnetic stirrer for uniform mixing. At specified intervals from 10 to 120 minutes, one flask was retrieved, and its suspension was filtered through Whatman No. 42 filter paper. The residual metal concentrations in the filtrate were determined as described in Section 2.4, and the adsorbed metal amount at time t (qt) was calculated using Equation (1).

$$q_t = q_e (1 - e^{-k1t}) \quad \ldots(4)$$

Where:

- q_t (mg.g^{-1}) is the amount of cadmium adsorbed at time ttt,
- q_e (mg.g^{-1}) is the adsorption capacity at equilibrium,
- k_1 (1.min^{-1}) is the pseudo-first-order rate constant.

The pseudo-second-order model is given by:

$$q_t = \frac{K_2 q_e^2 t}{1 + k_2 q_e t} \quad \ldots(5)$$

2.7. Error Analysis

To assess the accuracy and reliability of the isotherm and kinetic models, the root mean square error (RMSE) was used to compare experimental and predicted adsorption capacities. RMSE offers a direct measure of the average deviation between observed and calculated values, providing a more dependable evaluation of model performance than the coefficient of determination (R^2) alone. The calculation was performed using the following equation:

$$\text{Root mean square error (RMSE)} = \sqrt{\frac{1}{N}\sum_{i=1}^{N}(q_{e,exp} - q_{e,cal})^2} \quad \ldots(6)$$

Where $q_{e,exp}$ and $q_{e,cal}$ (mg.g^{-1}) are the experimental and calculated adsorption capacities, respectively, and N is the number of experimental data points. Lower RMSE values indicate better agreement between experimental and predicted results.

3. RESULTS AND DISCUSSION

3.1. Adsorbent Characteristics

The FTIR spectra of banana peel powder (BP), Fe_3O_4, and TiO_2 nanoparticles before and after adsorption are shown in Fig. 2a–b. In the BP spectrum, a broad band around 3400 cm⁻¹ indicates O–H stretching from hydroxyl groups in cellulose, hemicellulose, and lignin. Peaks near 2920 cm⁻¹ correspond to aliphatic C–H stretching. Absorption bands between 1655–1560 cm⁻¹ and 1250–1020 cm⁻¹ represent C=O/C=C and C–O stretching vibrations, highlighting the presence of functional groups capable of binding metal ions.

The Fe_3O_4 spectrum features a broad O–H band near 3400 cm⁻¹ and a strong Fe–O stretching vibration between 550 and 480 cm⁻¹, confirming the formation of magnetite nanoparticles. TiO_2 shows characteristic Ti–O–Ti vibrations around 745 cm⁻¹ and Ti–O vibrations between 480 and 500 cm⁻¹, indicating its crystalline structure.

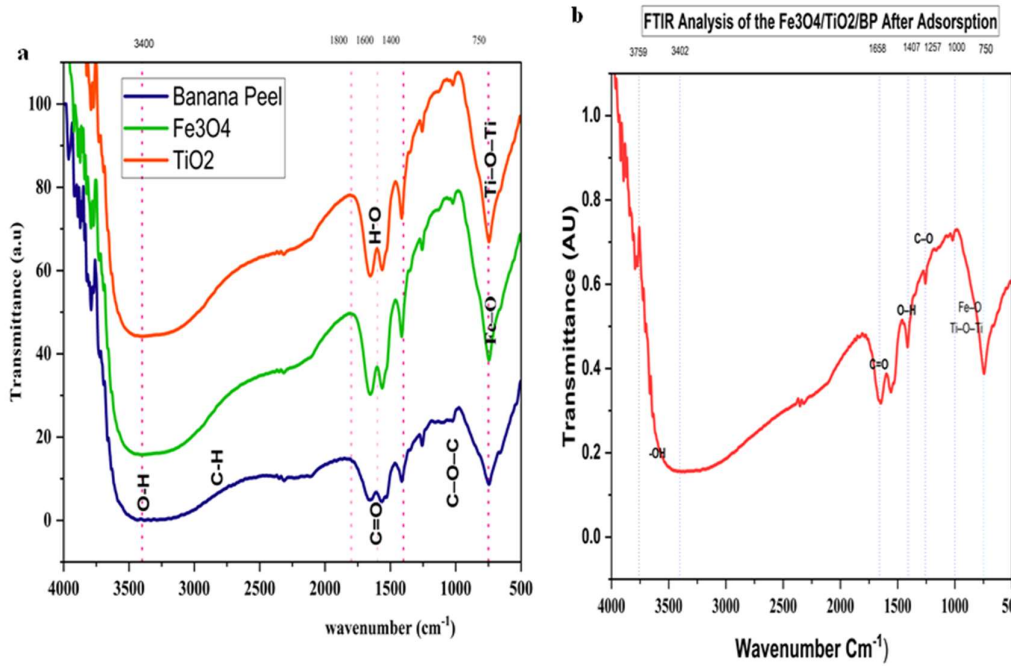

Fig. 2: FTIR spectrum of the materials (a) before adsorption, (b) after adsorption.

Following adsorption, the spectrum of the Fe_3O_4/TiO_2/BP nanocomposite reveals significant changes in band intensity and position. The broad O–H band (3759–3402 cm^{-1}) diminishes in intensity and shifts slightly, suggesting hydroxyl groups participate in metal binding via hydrogen bonding or ion exchange. Peaks at 1658 cm^{-1}, 1407 cm^{-1}, and 1257 cm^{-1} correspond to C=O, carboxylate, and C–O vibrations, implying their involvement in metal ion complexation. The Fe–O and Ti–O bands (1000–750 cm^{-1}) remain evident, demonstrating the structural stability of the composite after adsorption.

The observed spectral changes demonstrate that hydroxyl, carbonyl, and carboxyl functional groups play key roles in metal ion adsorption onto the Fe_3O_4/TiO_2/BP nanocomposite surface.

The XPS analysis of iron oxide (Fig. 3a–b) reveals distinct signals from Fe2+ 2p3/2 (~708.5 eV) and Fe3+ 2p3/2

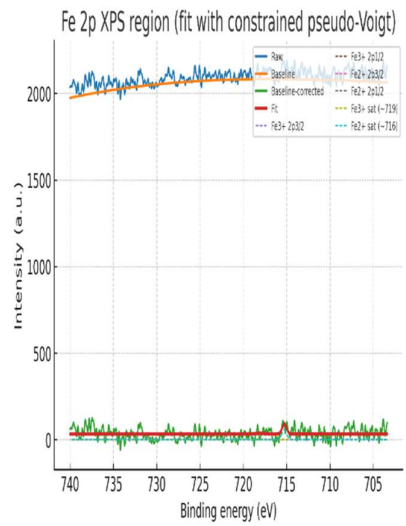

Fig. 3a: Fe 2p XPS region of iron oxide.

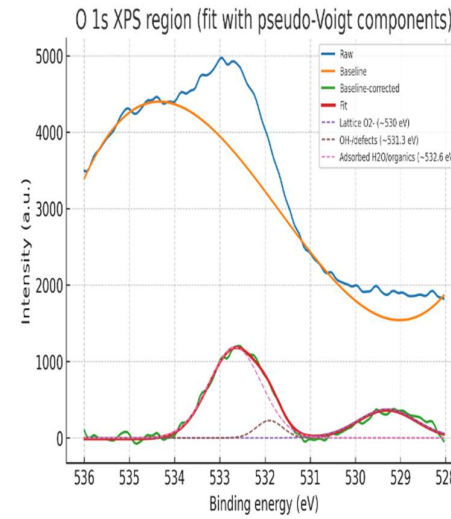

Fig. 3b: O1s XPS region of iron oxide.

Table 1: Fitted parameters of XPS analysis on iron oxide.

Component	Area [a.u.]	Position [eV]	Sigma [eV]	Eta [0-1]	Fe^{3+} fraction [from 2p3/2]
Fe^{3+} 2p3/2	1.3E-12	711.9803	1.799834	0.999183	4.88E-07
Fe^{3+} 2p1/2	6.51E-13	725.0803	1.799834	0.999183	4.88E-07
Fe^{2+} 2p3/2	2.67E-06	708.5125	1.773371	0.970402	4.88E-07
Fe^{2+} 2p1/2	1.33E-06	721.6125	1.773371	0.970402	4.88E-07
Fe^{3+} sat	5.626487	718	0.434943	1.17E-13	4.88E-07
Fe^{2+} sat	37.82937	715.2522	0.260823	4.59E-31	4.88E-07

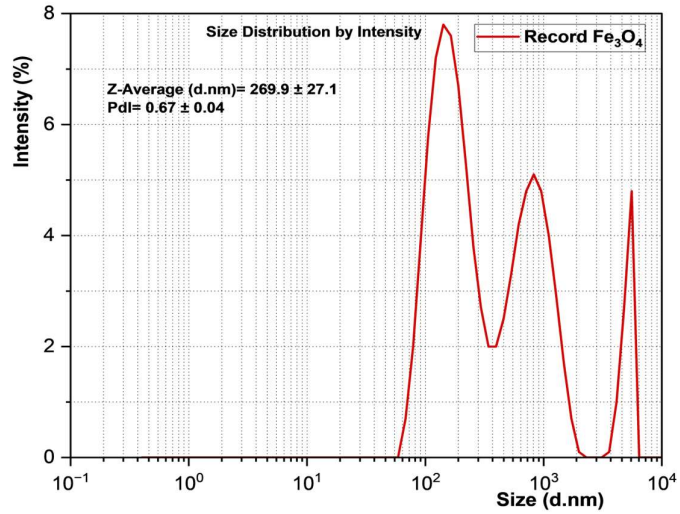

Fig. 4: Particle size distribution curve of iron oxide measured by Dynamic Light Scattering.

(~712.0 eV), along with their spin–orbit counterparts (ΔE ≈ 13.1 eV, ratio 2:1). Shake-up satellite peaks appear around 716 eV and 719 eV. All binding energies were calibrated to the C 1s peak at 285.0 eV, with fitted parameters summarized in Table 1. The O 1s spectrum (Fig. 3b) was deconvoluted into three components: lattice oxygen (O^{2-}, ~529.3 eV), hydroxyl groups or oxygen vacancies (~531.9 eV), and adsorbed water or organic species (~532.7 eV). Survey scans confirmed the presence of C 1s, Fe 2p, O 1s, S 2p, and Ti 2p peaks in both the iron oxide and banana peel-derived samples. The Fe 2p doublets of a standard Fe2O3 sample served as references for oxidation state determination.

The XPS results confirm the coexistence of Fe^{2+} and Fe^{3+} species, together with surface hydroxyl and oxygen defect sites, which are expected to play a crucial role in adsorption and surface reactivity (Table 1).

The particle size distribution of the synthesized Fe_4O_4 iron oxide was characterized using a HORIBA SZ-100 nanoparticle analyzer (HORIBA Scientific, Japan) based on dynamic light scattering (DLS). Measurements were taken in a transparent four-sided cuvette with a 10 mm optical path. As illustrated in Fig. 4, the intensity-weighted size distribution is broad and multimodal, indicating aggregation of particles in aqueous suspension. A significant peak appears at approximately 1593 nm, with other larger sizes suggesting the formation of agglomerates. The Z-average hydrodynamic diameter (~3432 nm) significantly exceeds the modal size, highlighting the sensitivity of cumulant-based DLS analysis to larger aggregates. The polydispersity index (PDI) of 0.67 indicates a highly polydisperse system. Although the primary particles are nanoscale, magnetic dipole–dipole interactions induce aggregation in water, meaning the reported particle sizes reflect hydrodynamic diameters of clusters rather than the primary nanoscale dimensions.

The surface morphology of the synthesized iron oxide (Fig. 5a–d) primarily consists of irregular, agglomerated particles, a common trait of nanoscale iron oxides caused by strong magnetic forces and high surface energy. Higher magnification SEM images show that these agglomerates are made up of fine primary nanoparticles, nanoscale in size, clustered into larger secondary structures. This aligns with the SEM and DLS findings, where SEM depicts the morphology and size of primary particles in dry conditions, while DLS measures the hydrodynamic diameter of particle clusters in suspension. The presence of nanoscale primary particles offers a high surface area, beneficial for adsorption.

EDS analysis (Fig. 5e) indicates that Fe and O are the main elements, confirming iron oxide formation. Minor carbon signals likely originate from residual organics or carbon coating from SEM sample preparation. The lack of significant impurity peaks suggests the material is of high purity.

The SEM images (Fig. 6a–e) reveal that the synthesized TiO_2 particles have irregular morphologies, mainly composed of rod-like and granular structures with rough surfaces. These particles are densely packed and tend to form clusters, a typical characteristic of TiO_2 nanoparticles due to their high surface energy. The micrographs also show size variations, indicating a polydisperse sample (Suttiponparnit et al. 2011). The EDS spectrum (Fig. 6f) verifies the presence of titanium (Ti) and oxygen (O) as the primary elements, confirming the successful formation of TiO_2 nanoparticles. Minor peaks for C, Na, and Si are also detected, likely arising from the supporting substrate, residual precursors, or surface contamination. Overall, these findings confirm the effective synthesis of TiO_2 nanoparticles with a nanostructured morphology and characteristic elemental composition, suitable for adsorption applications.

The SEM images of banana peel (Fig. 7a–c) depict a heterogeneous, rough, and fibrous surface characteristic of lignocellulosic biomass. The micrographs display layered, wrinkled textures with porous, fibrillar networks, indicating numerous cavities and irregular channels that function as potential adsorption sites. These morphological features, combined with a surface area of approximately 13 $m^2.g^{-1}$, improve the accessibility of active sites and

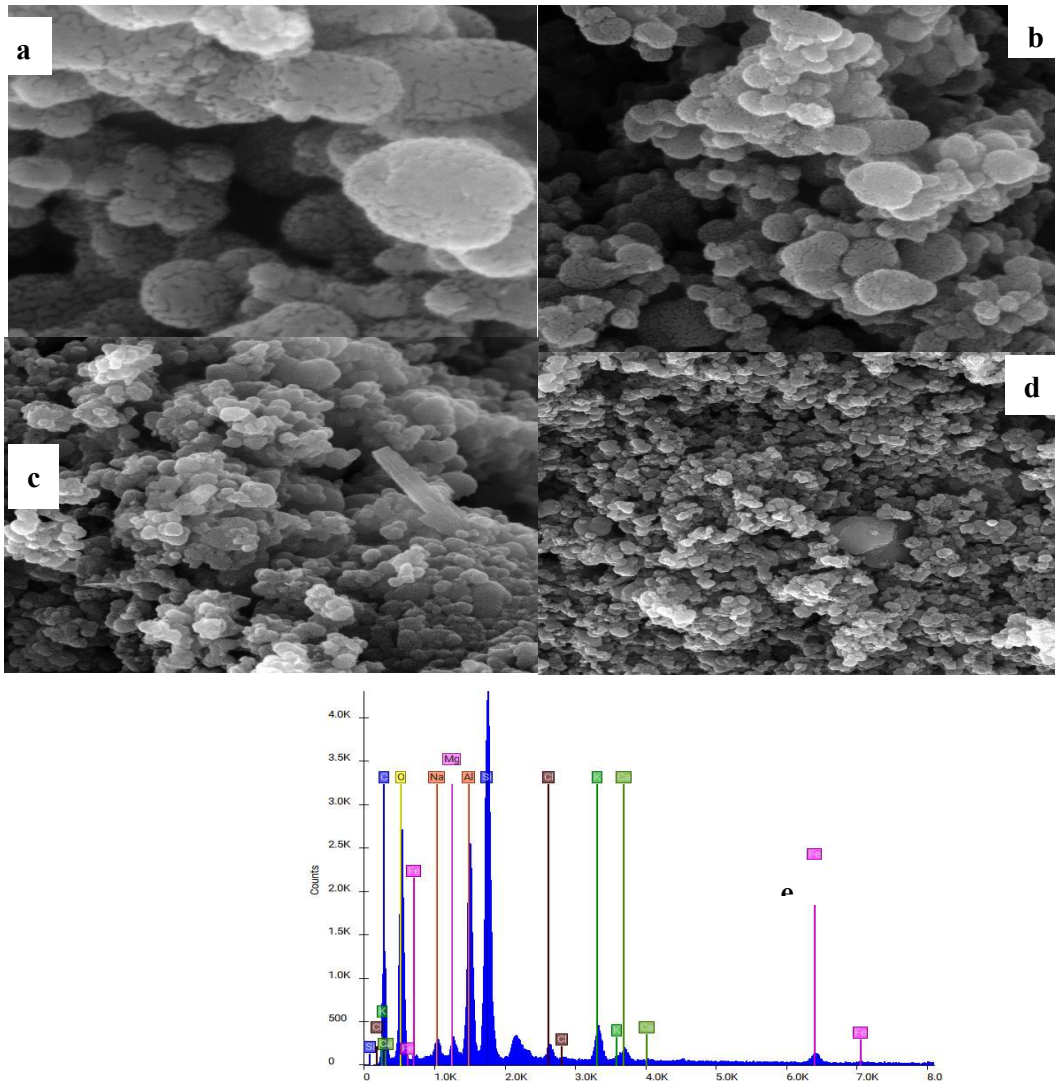

Fig. 5a-e: Scanning electron microscopy of iron oxide.

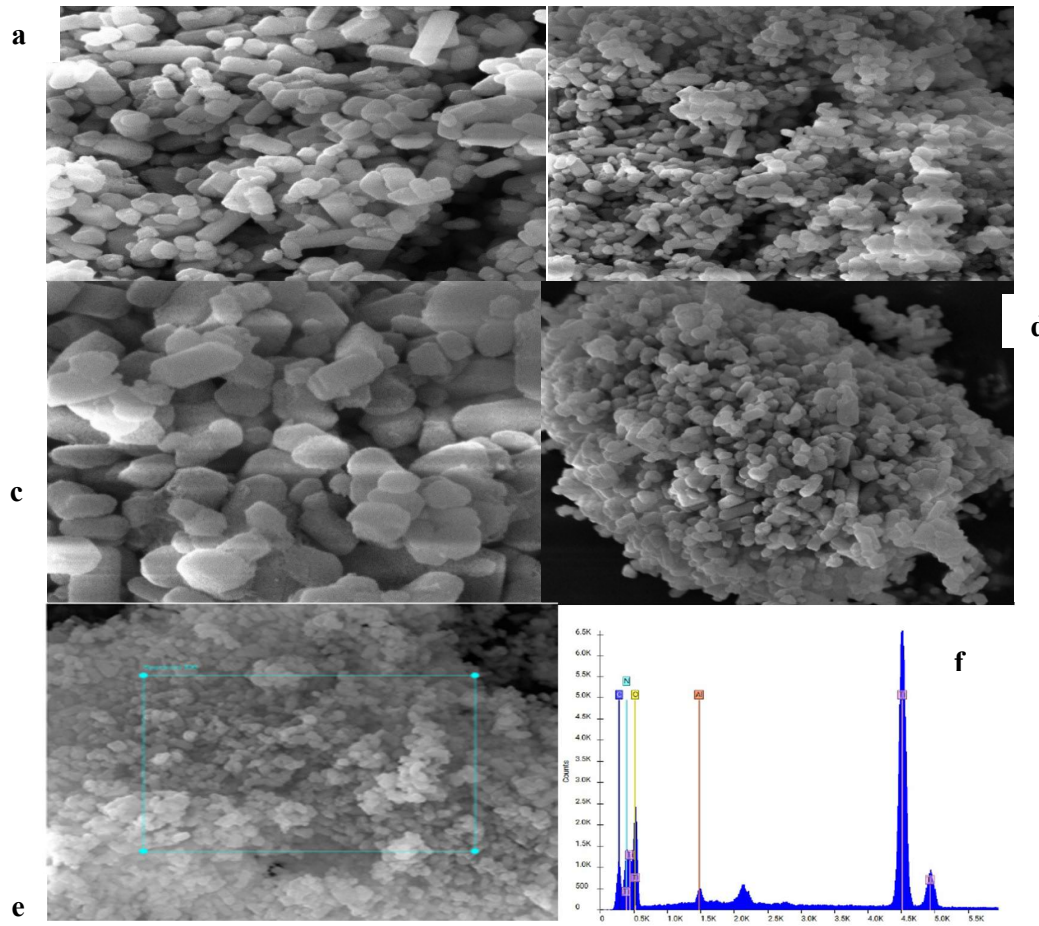

Fig. 6: SEM micrographs and EDS spectrum of titanium dioxide (TiO2) adsorbent.

promote pollutant diffusion within the adsorbent matrix. The EDS spectrum (Fig. 7d) confirms that carbon (C) and oxygen (O) are the predominant elements, consistent with the presence of cellulose, hemicellulose, and lignin, along with minor inorganic elements from the natural biomass or introduced during activation. Overall, SEM–EDS analysis demonstrates that the banana peel-based adsorbent exhibits a rough, porous structure, moderate surface area, and diverse elemental composition, making it an effective and sustainable material for adsorption and water purification.

3.1.4. Surface Area and Porosity Analysis (BET/BJH)

The surface area and pore characteristics of Fe_3O_4, TiO_2, and banana peel were analyzed using nitrogen adsorption–desorption (BET/BJH) at 77 K (Fig. 8). The isotherms display type IV behavior with hysteresis loops, indicating mesoporous structures. Fe_3O_4 exhibited a high BET surface area of 342.10 $m^2.g^{-1}$, a total pore volume of 0.432 $cm^3.g^{-1}$, and an average pore diameter of 2.94 nm, confirming its mesoporous, nanoscale features. TiO_2 showed a surface area of 172.44 $m^2.g^{-1}$, a pore volume of 0.448 $cm^3.g^{-1}$, and an average pore diameter of 9.96 nm, also within the mesoporous range. Conversely, banana peel had a significantly lower surface area of 22.94 $m^2.g^{-1}$ and pore volume of 0.019 $cm^3.g^{-1}$, consistent with its biomass origin. The high surface areas and nanoscale pore sizes of Fe_3O_4 and TiO_2 support the presence of nanoscale primary particles observed by SEM.

3.1.5. Zeta Potential

Zeta potential analysis was performed to assess the surface charge properties and colloidal stability of the adsorbent materials. As illustrated in Fig. 9, banana peel (BP) displayed a highly negative zeta potential of −29.2 mV, indicating robust electrostatic stability in aqueous suspension. This negative charge is mainly due to the presence of oxygen-containing functional groups such as carboxyl and hydroxyl groups on the banana peel surface. Conversely, TiO_2 and Fe_3O_4 showed low positive zeta potentials of +7.21 mV and +13.5 mV, respectively, implying limited colloidal stability and a higher likelihood of particle aggregation in water. The more negative surface charge of BP underscores

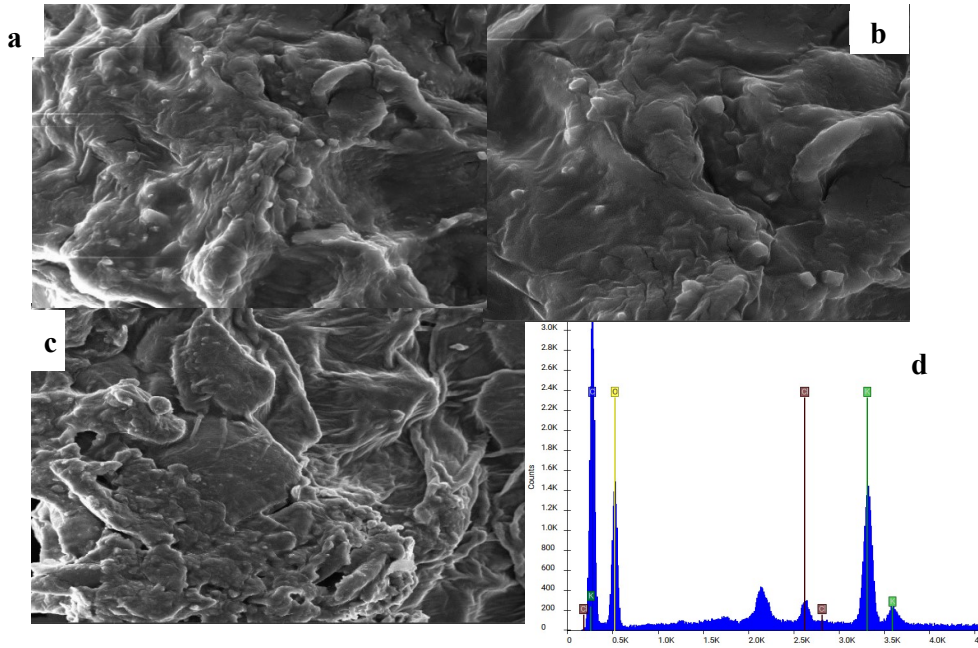

Fig. 7a-d: SEM micrographs and EDS spectrum of banana peel (BP)-based. adsorbent.

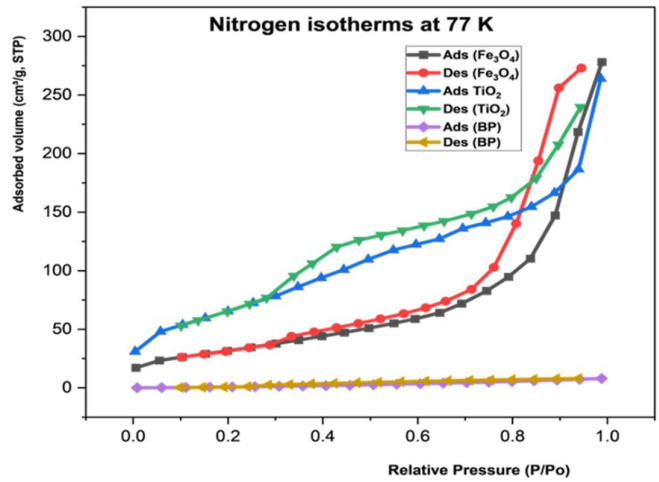

Fig 8: N_2 adsorption-desorption isotherms and BJH/BET textural parameters of the materials at 77 K.

its potential to improve surface stability and the adsorption efficiency of composites when combined with inorganic nanoparticles. These results validate the use of banana peel as a biopolymeric modifier to enhance the dispersion and electrostatic characteristics of Fe_3O_4- and TiO_2-based adsorbents for water and wastewater treatment.

3.1.6. VSM Analysis

The magnetic properties of iron oxide and TiO_2 were examined using a vibrating sample magnetometer (VSM). The hysteresis loop of iron oxide (Fig. 10) displays a narrow S-shaped curve with low coercivity (Hc $\approx$ 80–120 Oe) and minimal remanent magnetization (Mr $\approx$ 5–10 $\times$ 10^{-5} emu.g^{-1}), indicating weak ferrimagnetic behavior. The saturation magnetization (Ms) was found to be approximately 0.0025 emu.g^{-1}. The low Ms value suggests the material has a weak magnetic response, likely due to surface modification and dilution of the magnetic phase within the composite. As a result, the material shows limited magnetic responsiveness rather than practical magnetic separation, and magnetic recovery would only be achievable with a strong external magnetic field at close range (Selim et al. 2023).

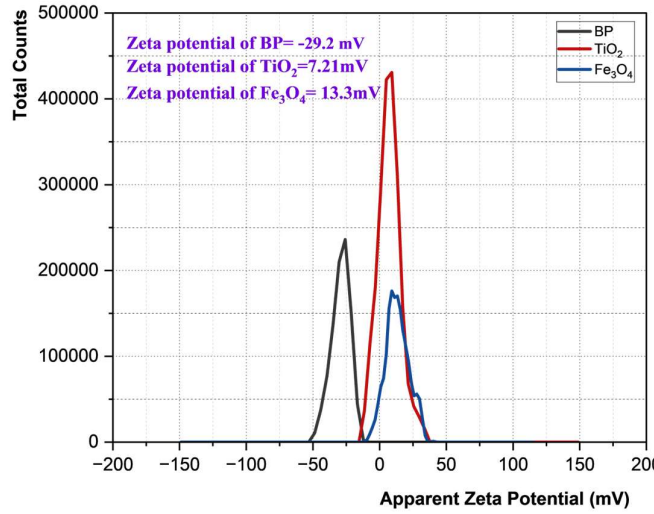

Fig. 9: Zeta potential distribution of Fe_3O_4/TiO_2/BP nanoparticles.

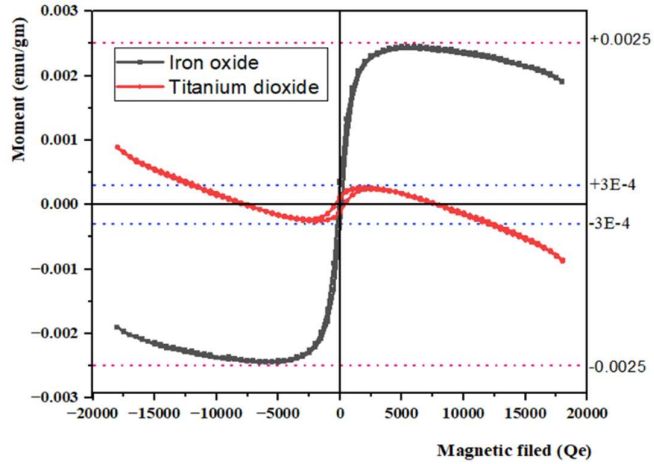

Fig. 10: VSM analysis of iron oxide and titanium dioxide.

Conversely, TiO_2 exhibits an almost linear magnetization curve with negligible coercivity and remanent magnetization, confirming its nonmagnetic nature. Although TiO_2 does not influence the magnetic properties of the composite, its addition enhances the overall adsorption capacity.

3.2. Adsorption Isotherms

The equilibrium adsorption data were modeled using the nonlinear Langmuir, Freundlich, Temkin, and Redlich–Peterson isotherm models (Fig. 11a–e, Table 2) to explore how Cr(VI), Cd(II), and Pb(II) interact with the Fe_3O_4/TiO_2/banana peel nanocomposite. Adsorption efficiency increased with higher adsorbent doses, peaking at 2.0 g, which indicates more active sites are available for metal ion uptake (Foroutan et al. 2022). For Cr(VI), both the Langmuir (R^2 = 0.729, qmax = 14.40 $mg.g^{-1}$) and Freundlich (R^2 = 0.75, KF = 7.12, 1/n = 0.47) models yielded moderate fits, pointing to a mixed adsorption process involving partial monolayer adsorption on a heterogeneous surface. The Freundlich constant (1/n < 1) signifies favorable adsorption. The Redlich–Peterson model (R^2 = 0.73, β = 0.51) further supports this mixed mechanism. For Cd(II), all isotherm models showed low correlation coefficients ($R^2 \leq 0.20$), while for Pb(II), several models produced statistically invalid fits, including negative R^2 values. These outcomes are likely due to nearly complete (~100%) removal efficiencies during experiments, causing equilibrium concentrations to approach zero. Under such conditions, standard adsorption isotherm models cannot reliably fit the data because a clear equilibrium adsorption curve is lacking. Therefore, no definitive adsorption mechanism can be determined for Cd(II) or Pb(II) based on these models, and the parameters should be interpreted with caution.

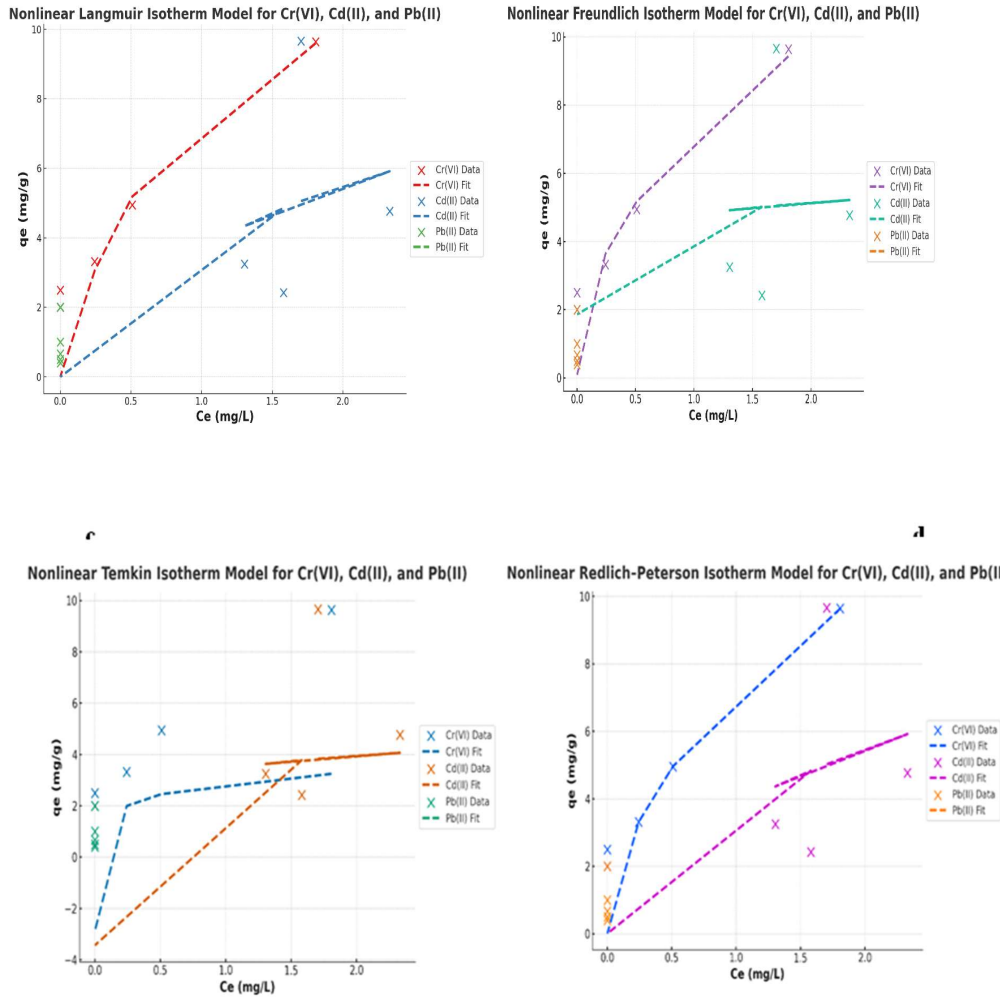

Fig. 11: Adsorption isotherm models (a-Nonlinear Langmuir, b-Nonlinear Freundlich, Nonlinear Temkin, and d-Nonlinear Redlich–Peterson) for the removal of metal ions onto Fe_3O_4/TiO/BP.

Table 2: Adsorption isotherm models and their parameters.

Model	Metal	Model Parameters	R^2	RMSE
Langmuir	Cr(VI)	Q_{max} = 14.3983 mg.g^{-1}, K_L = 1.10588 L.mg^{-1}	0.729	1.44
	Cd(II)	Q_{max} = 10.966 mg.g^{-1}, K_L = 0.50213 L.mg^{-1}	0.134	2.59
	Pb(II)	Q_{max} = 100 mg.g^{-1}, K_L = 10 L.mg^{-1}	-1.966	0.99
Freundlich	Cr(VI)	K_F = 7.12, 1.n^{-1} = 0.47	0.75	1.39
	Cd(II)	K_F = 4.78, 1.n^{-1} = 0.102	0.20	2.49
	Pb(II)	K_F = 27.15, 1.n^{-1} = 0.37	2.22E–	0.58
Temkin	Cr(VI)	AT = 100 L.g^{-1}, bT = 3962.954 J.moL^{-1}	-1.65	4.51
	Cd(II)	AT = 100 L.g^{-1}, bT = 3320.767 J.moL^{-1}	-0.70	3.63
	Pb(II)	AT = 100 L.g^{-1}, bT = 10000 J.moL^{-1}	-12.53	2.13
Redlich–Peterson	Cr(VI)	KR = 100 L.g^{-1}, aR = 13.10 L.mg^{-1}, β = 0.51	0.73	1.43
	Cd(II)	KR = 100 L.g^{-1}, aR = 25.34 L.mg^{-1}, β = 0.49	0.13	2.60
	Pb(II)	KR = 100 L.g^{-1}, aR = 2.99E–05 L.mg^{-1}, β = 1	-2.42	1.07

Overall, only Cr(VI) adsorption could be reasonably described by conventional isotherm models (Langmuir and Freundlich), whereas Cd(II) and Pb(II) exhibited adsorption behaviors beyond the applicability of the tested isotherm models.

The adsorption experiments were carried out in a multicomponent system where Cr(VI), Cd(II), and Pb(II) coexisted and competed for the same surface-active sites on the Fe_3O_4/TiO_2/BP nanocomposite. Consequently, their adsorption behaviors are interdependent and cannot be simply equated to those observed in single-metal systems. Differences in removal efficiency are influenced by factors such as ionic charge, hydrated ionic radius, polarizability, and aqueous speciation. Pb(II) demonstrated the highest affinity for the adsorbent, followed by Cd(II), while Cr(VI), mainly present as anions, showed comparatively weaker adsorption in competition. Although individual isotherm models were used for clarity, the results illustrate the competitive adsorption dynamics in multicomponent conditions. Detailed quantitative modeling of competitive adsorption was beyond this study's scope and should be explored in future research.

3.3. Kinetic Studies

The assessment of adsorbent dosage on adsorption kinetics aimed to simulate practical operating conditions rather than to determine fundamental kinetic constants. As the adsorbent dosage increased, the adsorption capacity (qe, $mg.g^{-1}$) decreased, likely due to a dilution effect and the underutilization of available surface-active sites at higher doses. This typical behavior in batch adsorption systems does not imply a reduction in overall adsorption efficiency or rate.

The kinetic parameters obtained at different adsorbent dosages are not directly compared as intrinsic constants. Instead, kinetic modeling was employed to describe adsorption trends and rate-controlling processes independently at each dosage condition

3.3.1. Kinetic Studies for Chromium (Cr(VI))

The adsorption kinetics of Cr(VI) onto the Fe_3O_4/TiO_2/BP nanocomposite were investigated to elucidate the rate-controlling mechanisms of ion removal. The adsorption capacity increased rapidly during the initial contact period (10–45 min), which can be attributed to the abundance of

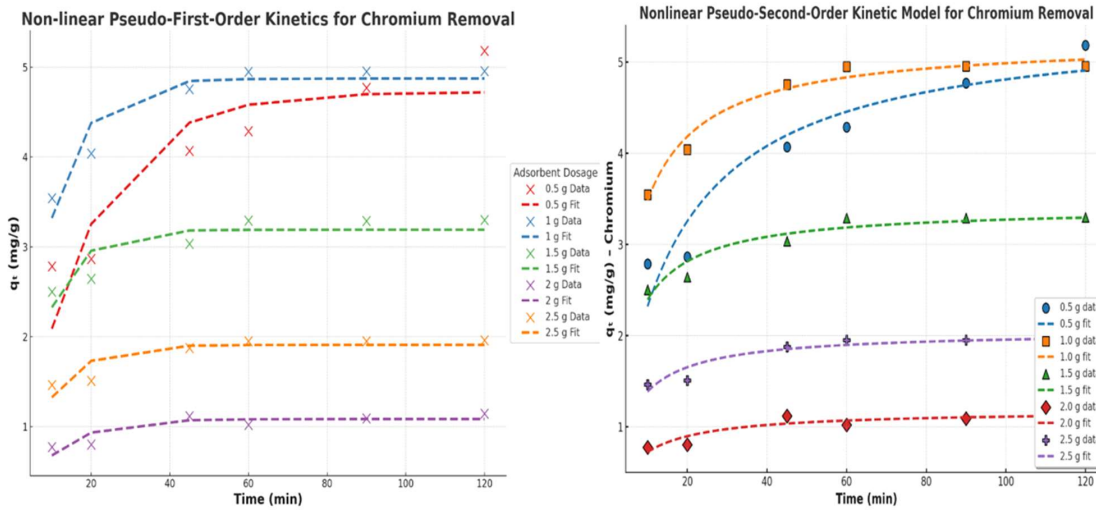

Fig. 12: Nonlinear pseudo-first-order and pseudo-second-order for chromium removal.

Table 3: Nonlinear fitted pseudo-first-order and pseudo-second-order kinetic models for the removal of Chromium ions using different masses of Fe_3O_4/TiO_2/BP.

Mass	Pseudo-first-order				Pseudo-second-order			
	qe [$mg.g^{-1}$]	k1	R^2	RMSE	qe [$mg.g^{-1}$]	k2	R^2	RMSE
0.5g	4.723	0.0584	0.785	0.416	5.46	0.013	0.90	0.286
1g	4.873	0.114	0.893	0.179	5.24	0.038	0.97	0.086
1.5g	3.191	0.131	0.712	0.174	3.41	0.07	0.91	0.1
2g	1.084	0.098	0.735	0.077	1.18	0.133	0.84	0.06
2.5g	1.91	0.118	0.73	0.111	2.05	0.10	0.89	0.071

available surface-active sites and favorable electrostatic interactions between Cr(VI) anions and the positively charged surface of the nanocomposite. As the adsorption process progressed, the uptake rate gradually decreased and eventually reached equilibrium as the available active sites became increasingly occupied, thereby reducing the driving force for mass transfer.

The kinetic data were analyzed using the pseudo-first-order (PFO) and pseudo-second-order (PSO) models (Fig. 12, Table 3). The PSO model provided a better fit to the experimental data, as indicated by higher correlation coefficients (R^2 = 0.84–0.97) and lower RMSE values than those obtained with the PFO model. These results suggest that the adsorption process is predominantly governed by surface-related interactions and the availability of active sites, with chemisorption serving as the primary rate-controlling mechanism rather than diffusion alone.

3.3.2. Kinetic Studies for Cadmium(II)

The time-dependent adsorption of Cd(II) onto Fe_3O_4/TiO_2/BP was examined to evaluate the adsorption rate and controlling processes. Rapid adsorption occurred within the first 20–40 min, corresponding to the occupation of the surface-active sites. As equilibrium was approached, the adsorption rate slowed, likely due to site saturation and increased resistance to mass transfer.

Kinetic modeling using the PFO and PSO equations (Fig. 13, Table 4) showed that the PSO model provided a better fit to the experimental data (R^2 = 0.75, RMSE = 0.0068) than the PFO model. This indicates that Cd(II) adsorption kinetics are influenced by surface interactions and active-site availability. At higher adsorbent dosages, equilibrium was reached more rapidly, which limited the applicability of kinetic modeling under these conditions.

3.3.3. Kinetic Studies for Lead (Pb(II))

The adsorption of Pb(II) onto the Fe_3O_4/TiO_2/BP nanocomposite demonstrated a rapid initial phase, followed by a more gradual approach to equilibrium. This initial fast stage indicates a strong affinity of Pb(II) ions for surface-active sites, while the subsequent slower phase may be due to site saturation and diffusion limitations. Kinetic analysis using the PFO and PSO models (Fig. 14, Table 5) showed that the PSO model best fitted the experimental data, with higher correlation coefficients (R2= 0.87–0.95) and lower RMSE values. This indicates that Pb(II) adsorption kinetics are predominantly governed by surface interactions rather than simple physical diffusion.

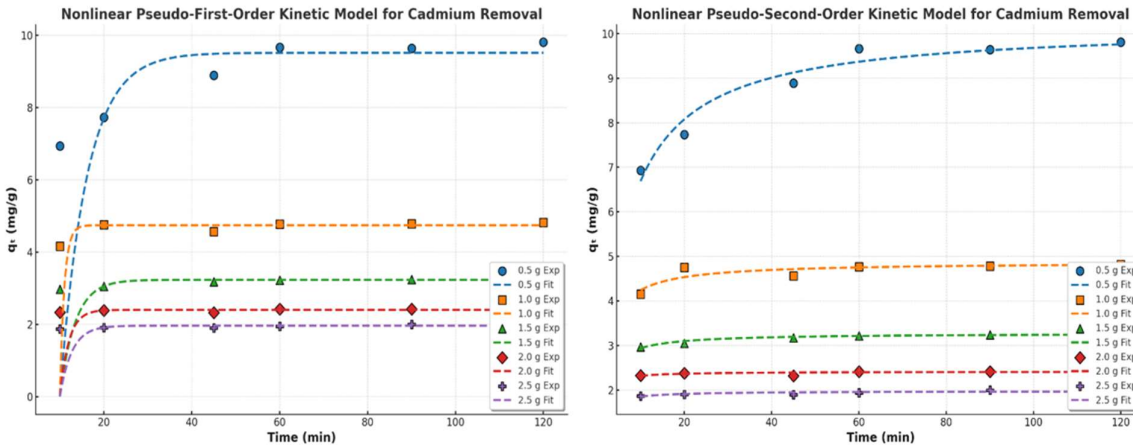

Fig. 13: Nonlinear pseudo-first-order and pseudo-second-order models for cadmium removal.

Table 4: Nonlinear fitted pseudo-first-order and pseudo-second-order kinetic models for the removal of Cadmium ions using different masses of Fe_3O_4/TiO_2/BP.

Mass	Pseudo-first-order				Pseudo-second-order			
	qe [mg.g^{-1}]	k_1 [1.min^{-1}]	R^2	RMSE	qe [mg.g^{-1}]	k_2	R^2	RMSE
0.5g	9.43	0.11	0.82	0.46	10.18	0.019	0.95	0.23
1g	4.75	0.21	0.86	0.09	4.87	0.14	0.76	0.114
1.5g	3.20	0.25	0.64	0.06	3.28	0.27	0.93	0.028
2g	2.40	0.36	0.29	0.037	2.42	1	0.41	0.034
2.5g	1.95	0.31	0.38	0.04	1.98	0.76	0.63	0.03

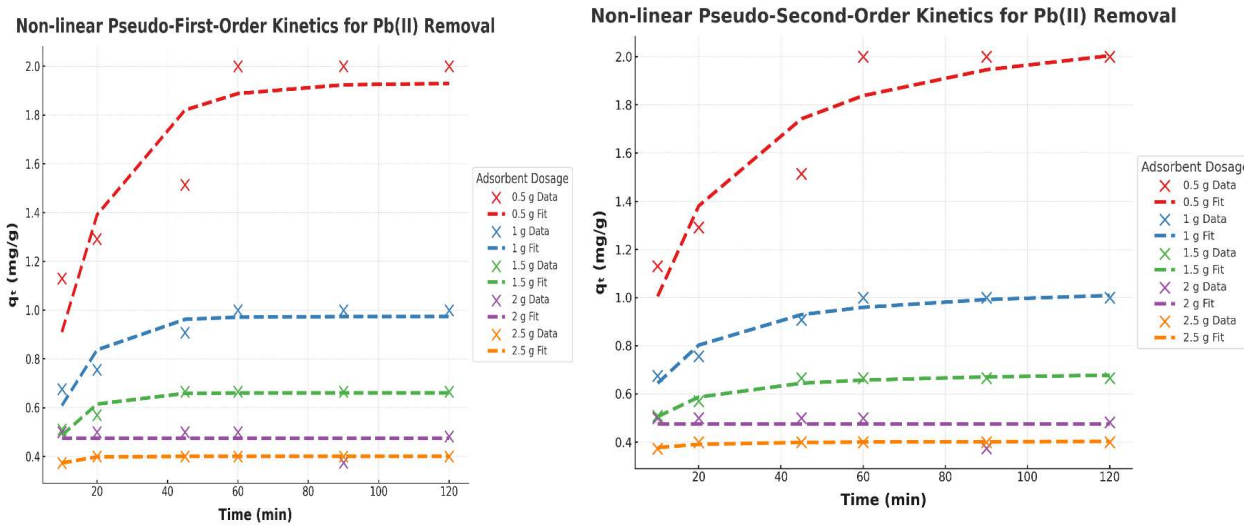

Fig. 14: Nonlinear pseudo-first-order and pseudo-second-order for lead removal.

Table 5: Nonlinear fitted pseudo-first-order and pseudo-second-order kinetic models for the removal of lead ions using different masses of Fe_3O_4/TiO_2/BP.

Mass	Pseudo-first-order				Pseudo-second-order			
	qe [mg.g^{-1}]	k_1 [1.min^{-1}]	R^2	RMSE	qe [mg.g^{-1}]	k_1 [1.min^{-1}]	R^2	RMSE
0.5g	1.93	0.06	0.78	0.17	2.203	0.038	0.87	0.13
1g	0.97	0.1	0.84	0.05	1.06	0.144	0.95	0.03
1.5g	0.66	0.134	0.88	0.02	0.7	0.37	0.96	0.013
2g	0.48	1	~0.00	0.05	0.51	1	~0.00	0.062
2.5g	0.40	0.27	0.99	0.0006	0.43	3.32	0.808	0.017

Different experimental runs were performed to assess how adsorbent dosage influences the rate of adsorption. Typically, the PSO kinetic rate increased with higher dosages. To evaluate the model's accuracy, the equilibrium adsorption capacity predicted by the PSO model at a specific dosage should be compared with the actual batch experimental data obtained at the same dosage. Notably, the equilibrium adsorption capacities tend to decrease as adsorbent dosage increases, likely due to the greater number of available sites, considering the initial heavy metal concentration remains constant.

3.4. Comparative Evaluation with Reported Adsorbents

The Fe_3O_4/TiO_2/BP nanocomposite exhibited high adsorption capacities for Cr(VI), Cd(II), and Pb(II), confirming the synergistic effect of Fe_3O_4 and TiO_2 nanoparticles supported on banana peel biomass. The maximum adsorption capacities of 10.9 mg.g^{-1} for Cd(II) and 100 mg.g^{-1} for Pb(II) obtained in this study are significantly higher than that of raw banana peel (~5.9 mg.g^{-1}) reported by Deshmukh et al. (2017) and are comparable to that of BPB/Fe_3O_4 (~30.3 mg.g^{-1}) reported in the same study. The adsorption performance also remains competitive with more advanced composites, such as BPAC/Al_2O_3–chitosan (~46.9 mg.g^{-1}) and BPB/Fe_3O_4/ZIF-67 (~50.8 mg.g^{-1}), reported by Ramutshatsha-Makhwedzha et al. (2022). Kinetic analysis revealed that adsorption followed the pseudo-second-order (PSO) model, particularly at the 2 g adsorbent dosage, with R^2 values ranging from 0.89 to 0.99 and low RMSE values, indicating that chemisorption, involving electron exchange or complexation with oxygen-containing functional groups, was the predominant adsorption mechanism. Compared with Fe_3O_4–*Actinomucor* sp. composites (qmax = 29.5 mg.g^{-1}) reported by Masoudi et al. (2018), the Fe_3O_4/TiO_2/BP nanocomposite demonstrated superior adsorption capacity while exhibiting similar kinetic behavior.

These findings demonstrate that the Fe_3O_4/TiO_2/BP nanocomposite achieves a favorable balance between adsorption efficiency, structural stability, and a simple, environmentally friendly synthesis route, making it a promising low-cost adsorbent for the removal of heavy metals from aqueous systems.

5. CONCLUSIONS

This study successfully synthesized and evaluated a Fe_3O_4/TiO_2/banana peel (BP) nanocomposite for removing Cr(VI),

Cd(II), and Pb(II) from water. Characterization confirmed the presence of functionalized magnetic surfaces with high reactivity and structural stability. Adsorption data fit best with the Langmuir and Redlich–Peterson models, suggesting that metal ions were primarily adsorbed as a monolayer on uniform active sites. Kinetic results aligned with the pseudo-second-order model, indicating that chemisorption involving valence forces or surface complexation controlled the process. The maximum adsorption capacities—14.4 $mg.g^{-1}$ for Cr(VI), 10.9 $mg.g^{-1}$ for Cd(II), and 100 $mg.g^{-1}$ for Pb(II)—were comparable to or better than those of similar nanocomposites. These findings show that the Fe_3O_4/TiO_2/BP nanocomposite is an effective, magnetically separable, and eco-friendly material for heavy metal removal, promising for water treatment applications and sustainable waste utilization.

6. REFERENCES

Deshmukh, P.D., Khadse, G.K., Shinde, V.M. and Labhasetwar, P., 2017. Cadmium removal from aqueous solutions using dried banana peels as an adsorbent: Kinetics and equilibrium modeling. *Journal of Bioremediation & Biodegradation*, 8(3), p.1000395. [DOI]

FAO of the United Nations, 2024. FAO Statistical Yearbook 2024 reveals critical insights on the sustainability of global agriculture, food security, and the importance of agrifood systems in employment. *2024 Statistical Yearbook*, 2024. [DOI]

Foroutan, R., Peighambardoust, S.J., Mohammadi, R., Peighambardoust, S.H. and Ramavandi, B., 2022. Cadmium ion removal from aqueous media using banana peel biochar/Fe_3O_4/ZIF-67. *Environmental Research*, 211, p.113020. [DOI]

Gupta, S.S., Al Kausor, M. and Chakrabortty, D., 2025. Banana peel as potential bioadsorbent toward removal of emerging contaminants from wastewater for sustainable environment: A review. *Chemical Papers*, 79(5), pp.2717-2750. [DOI]

Keerthana, B.G.T., Solaiyammal, T., Muniyappan, S. and Murugakoothan, P., 2018. Hydrothermal synthesis and characterization of TiO_2 nanostructures prepared using different solvents. *Materials Letters*, 220, pp.20-23. [DOI]

Lellala, K., Behera, S.K., Srivastava, P., Saeed, W.S., Haidyrah, A.S. and Burile, A.N., 2024. Fe_3O_4 nanoparticles decorated on N-doped graphene oxide nanosheets for elimination of heavy metals from industrial wastewater and desulfurization. *Diamond and Related Materials*, 150, p.111746. [DOI]

Liew, R.K., Nam, W.L., Chong, M.Y., Phang, X.Y., Su, M.H., Yek, P.N.Y., Ma, N.L., Cheng, C.K., Chong, C.T. and Lam, S.S., 2018. Oil palm waste: An abundant and promising feedstock for microwave pyrolysis conversion into good quality biochar with potential multi-applications. *Process Safety and Environmental Protection*, 115, pp.57-69. [DOI]

Masoudi, R., Moghimi, H., Azin, E. and Taheri, R.A., 2018. Adsorption of cadmium from aqueous solutions by novel Fe3O4- newly isolated Actinomucor sp. bio-nanoadsorbent: Functional group study. *Artificial Cells, Nanomedicine and Biotechnology*, 46(sup3), pp.S1092-S1101. [DOI]

Mehmood, K. and Dhanya, W.M., 2025. Unlocking the potential of banana peel bioactives: Extraction methods, benefits, and industrial applications. *Discover Food*. [DOI]

Mishra, A., Kumari, M., Swati, Kumar, R., Iqbal, K. and Thakur, I.S., 2022. Persistent organic pollutants in the environment: Risk assessment, hazards, and mitigation strategies. *Bioresource Technology Reports*, 19, p.101143. [DOI]

Mishra, S., Prabhakar, B., Kharkar, P.S. and Pethe, A.M., 2023. Banana peel waste: An emerging cellulosic material to extract nanocrystalline cellulose. *ACS Omega*, 8(1), pp.8-13. [DOI]

Mor, S. and Ravindra, K., 2023. Municipal solid waste landfills in lower- and middle-income countries: Environmental impacts, challenges and sustainable management practices. *Process Safety and Environmental Protection*, 174, pp.510-530. [DOI]

Otieno, A.O., Home, P.G., Raude, J.M., Murunga, S.I., Ngumba, E., Ojwang, D.O. and Tuhkanen, T., 2021. Pineapple peel biochar and lateritic soil as adsorbents for recovery of ammonium nitrogen from human urine. *Journal of Environmental Management*, 293, p.112794. [DOI]

Pokharel, P., Kwak, J.H., Ok, Y.S. and Chang, S.X., 2018. Pine sawdust biochar reduces GHG emissions by decreasing microbial and enzyme activities in forest and grassland soils in a laboratory experiment. *Science of the Total Environment*, 625, pp.1247-1256. [DOI]

Ramutshatsha-Makhwedzha, D., Mbaya, R. and Mavhungu, M.L., 2022. Application of activated carbon banana peel coated with Al2O3-chitosan for the adsorptive removal of lead and cadmium from wastewater. *Materials*, 15(3), p.860. [DOI]

Razzak, S.A., Faruque, M.O., Alsheikh, Z., Alsheikhmohamad, L., Alkuroud, D., Alfayez, A., Hossain, S.M.Z. and Hossain, M.M., 2022. A comprehensive review on conventional and biological-driven heavy metals removal from industrial wastewater. *Environmental Advances*, 7, p.100168. [DOI]

Selim, M.M., El-safty, S. and Tounsi, A., 2023. Review of the impact of the external magnetic field on the characteristics of magnetic nanofluids. *Alexandria Engineering Journal*, 76, pp.75-89. [DOI]

Sial, T.A., Khan, M.N., Lan, Z., Kumbhar, F., Ying, Z., Zhang, J., Sun, D. and Li, X., 2019. Contrasting effects of banana peels waste and its biochar on greenhouse gas emissions and soil biochemical properties. *Process Safety and Environmental Protection*, 122, pp.366-377. [DOI]

Smyth, S., 2024. Waste management in developing countries: Challenges and solutions. *Journal of Waste Management and Environmental Sustainability*, 9(3), p.350. [DOI]

Sossou, K., Bala Prasad, S., Agbotsou, K.E., Saidou Souley, H. and Mudigandla, R., 2024a. Characteristics of landfill leachate and leachate treatment by biological and advanced coagulation processes: Feasibility and effectiveness – An overview. *Waste Management Bulletin*, 2(2), pp.181-198. [DOI]

Sossou, K., Prasad, S.B., Agbotsou, E.K. and Saidou Souley, H., 2024b. Evaluation of the performance of magnetic zeolite nanocomposites in removing various water contaminants as heavy metals, organic pollutants, and emerging contaminants: A review. *Next Nanotechnology*, 6, p.100075. [DOI]

Strategies, E.F., Ayach, J., Malti, W.E., Duma, L., Lalev, J., Ajami, M.A., Hamad, H. and Hijazi, A., 2024. Comparing conventional and advanced approaches for heavy metal removal in wastewater treatment: An in-depth review. *Journal of Environmental Science and Technology*, 45(2), pp.112-128.

Suttiponparnit, K., Jiang, J., Sahu, M., Suvachittanont, S., Charinpanitkul, T. and Biswas, P., 2011. Role of surface area, primary particle size, and crystal phase on titanium dioxide nanoparticle dispersion properties. *Nanoscale Research Letters*, 6(1), p.27. [DOI]

Togun, H., Basem, A., Abdulrazzaq, T., Biswas, N., Abed, A.M., Dhabab, J.M., Mohammed, H.I., Sharma, B.K., Paul, D. and Barmavatu, P., 2025. Current developments in the use of nanotechnology to enhance the generation of sustainable bioenergy. *Sustainable Materials and Technologies*, 43, p.e01266. [DOI]

Zanganeh, S., Kajbafvala, A., Zanganeh, N., Molaei, R., Bayati, M.R., Zargar, H.R. and Sadrnezhaad, S.K., 2011. Hydrothermal synthesis and characterization of TiO_2 nanostructures using LiOH as a solvent. *Advanced Powder Technology*, 22(3), pp.336-339. [DOI]